

Structural properties of chalcogenide glasses and the isocoordination rule: Disentangling effects from chemistry and network topology

M. Micoulaut,¹ I. Pethes^{1b},² P. Jóvári^{1b},² L. Pusztai,^{2,3} M. Krbal,⁴ T. Wágner,^{4,5} V. Prokop,⁴ Š. Michalik^{1b},⁶ K. Ikeda,⁷ and I. Kaban^{1b}⁸

¹*Sorbonne Université, Laboratoire de Physique Théorique de la Matière Condensée, CNRS UMR 7600, 75252 Paris Cedex 05, France*

²*Institute for Solid State Physics and Optics, Wigner Research Center, H-1525 Budapest, POB 49, Hungary*

³*IROAST, Kumamoto University, 2-39-1 Kurokami, Chuo-ku, Kumamoto 860-8555, Japan*

⁴*Center of Materials and Nanotechnologies, Faculty of Chemical Technology, University of Pardubice, 6 Pardubice 53002, Czech Republic*

⁵*Department of General and Inorganic Chemistry, Faculty of Chemical Technology, University of Pardubice, Pardubice 53210, Czech Republic*

⁶*Diamond Light Source Ltd., Harwell Science and Innovation Campus, Didcot, Oxfordshire OX11 0DE, United Kingdom*

⁷*Institute of Materials Structure Science, High Energy Accelerator Research Organization (KEK), Tokai, Ibaraki 319-1106, Japan*

⁸*Leibniz-Institut für Festkörper- und Werkstofforschung Dresden, Institute for Complex Materials, 01069 Dresden, Germany*



(Received 25 April 2022; accepted 30 June 2022; published 19 July 2022)

The structural properties of two Ge-As-Se glass compositions ($\text{Ge}_{10}\text{As}_{10}\text{Se}_{80}$ and $\text{Ge}_{21}\text{As}_{21}\text{Se}_{58}$) are investigated from a combination of density-functional-based molecular dynamics simulations and neutron/x-ray scattering experiments. We first focus on structural characteristics, including structure factors, pair distribution functions, angular distributions, coordination numbers, and neighbor distributions, and compare our results with the experimental data. Results leave anticipated coordinations from the octet rule (Se^{II} , As^{III} , and Ge^{IV}) unchanged, and these are contrasted with respect to glasses having the same average coordination number \bar{r} such as binary $\text{As}_{30}\text{Se}_{70}$ and $\text{Ge}_{33}\text{Se}_{67}$. The increase of (As,Ge) content induces a growth of ring structures that are dominated by edge-sharing motifs (four-membered rings) having mostly heteropolar bonds, while As-As and As-Ge homopolar bonds are clearly more favored than Ge-Ge. These features signal that both topological (rings) and chemical (bonds) features are different with respect to related binaries. The validity of the so-called vibrational isocoordination rule stating that properties of multicomponent chalcogenides depend solely on \bar{r} is checked, and results from a vibrational analysis indicates that this rule is merely satisfied for the Se-rich composition. An inspection of correlations via the Bhatia-Thornton formalism shows that topological ordering is not only different between $\text{Ge}_{10}\text{As}_{10}\text{Se}_{80}$ and $\text{Ge}_{21}\text{As}_{21}\text{Se}_{58}$ but also radically contrasts with respect to the isocoordinated binary glasses and displays an obvious reduced directional bonding.

DOI: [10.1103/PhysRevB.106.014206](https://doi.org/10.1103/PhysRevB.106.014206)

I. INTRODUCTION

Chalcogenide glasses form a large variety of covalent systems that can be obtained from melt quenching. They offer wide possibilities of optoelectronic applications such as x-ray imaging, night-vision devices, infrared waveguides, or data storage. On a more basic side, these glasses form interesting model systems to test network effects such as topology or rigidity on physicochemical properties [1].

In Ge-As-Se glasses, a reasonable assumption using the so-called $8-\mathcal{N}$ rule (where \mathcal{N} is the number of outer shell electrons) permits to consider the structure as being made of twofold Se atoms ($n_{\text{Se}} = 2$), while As and Ge are respectively almost always 3- and 4-coordinated. On increasing Ge and As content x_{Ge} and x_{As} , the network average coordination number $\bar{r} = 2 + x_{\text{As}} + 2x_{\text{Ge}}$ increases and represents an attractive system variable that can be used to merge on a single representation various joins belonging to compositional space. For such systems, the presence of a possible “isocoordination”

rule has been detected [2,3], i.e., it has been observed that properties will stay constant for all compositions having the same \bar{r} . Examples showing this feature encompass the glass transition temperature [4], viscosity and related parameters [5,6], hardness, and vibrational density of states (VDOS) [7]. For the latter, it was shown that systems as different as As_2Se_3 and $\text{Ge}_{15}\text{As}_{30}\text{Se}_{55}$ show a similar VDOS in the transverse acoustic region [2].

Early numerical studies have attempted to check this rule for vibrational properties and simulations on bond depleted amorphous silicon have shown that this rule is not exact but holds qualitatively well over a wide range of compositions and local chemical correlations [8]. Conversely, the rule does not seem to be fulfilled for density [9], and for other measurements it has been recognized that chemical effects near the binary edges (Ge-Se and As-Se) might dominate [6]. For the present Ge-As-Se glasses, this poses the crucial question of the effect, combined or not, of network topology *via* \bar{r} and chemistry *via* composition and preferential chemical bonding.

It relates to topological versus chemical ordering which have been carefully considered for certain chalcogenides [10–13] and have led to the recognition of typical associated length scales.

Ge-As-Se glasses have received quite some attention due, in part, to the fact that they display flexible to rigid transitions [14]. The mean-field description of such transitions (i.e., Phillips-Thorpe rigidity theory [15,16]) is inspired by Maxwell elasticity theory of macroscopic structures [17]. At the molecular level, stretching and bending interactions constrain the atomic network and can be associated with mechanical constraints n_c which are compared to the available degrees of freedom [3 in three-dimensional (3D)]. This analysis shows that glasses with a low connectedness containing a large fraction of twofold chalcogens (Se) are flexible, whereas a network consisting of a large amount of (Ge,As) atoms is intrinsically rigid. The *locus* of the transition is identified with the so-called Maxwell isostatic stability criterion (i.e., $n_c = 3$), corresponding to a network with $\bar{r} = \bar{r}_c = 2.40$. Several experimental studies have shown that anomalies do appear close to \bar{r}_c in relaxation properties [6,18]. For the particular join $\text{Ge}_x\text{As}_x\text{Se}_{100-2x}$, with the assumed coordination number following the $8-\mathcal{N}$ rule, it is easy to check that the condition $n_c = 3$ or $\bar{r} = 2.4$ is satisfied for $x = x_c = 13.3\%$.

The structure of Ge-As-Se glasses has been investigated by different authors [19–23], sometimes in relationship with optical [18,24–26] or relaxation properties [18,26–31]. Among specific features, a dimensional change from a $D = 2$ to $D = 3$ network is suggested [32] at $\bar{r} = 2.45$, whereas nanoscale phase separation [33] is expected to occur at large connectedness ($\bar{r} = 2.60$). This is, however, contradicted from T_g measurements [34]. A compositional window [27] linked with flexible to rigid transitions is found for $9.5\% \leq x \leq 17.0\%$ in $\text{Ge}_x\text{As}_x\text{Se}_{100-2x}$ that displays a near reversible character of the glass transition with minimal changes in enthalpy together with weak space-filling tendencies (minimum of molar volume). These features are thought to be the manifestation of a topological (intermediate) phase that has been predicted from $T = 0$ rigidity models [35,36] and observed for a variety of chalcogenide and modified oxide glasses [37].

Regarding simulation work, we are only aware of a recent *ab initio* study on select compositions of Ge-As-Se glasses [38] that were obtained from prepared reverse Monte Carlo (RMC) atomic configurations. Results indicated that the assumption of the $8-\mathcal{N}$ rule for Ge-As and Se atoms was incorrect and Se poor systems were found to contain significant homopolar and non Se bonding, together with short Se chains.

Here we present a combined study using density-functional-theory- (DFT) based molecular dynamics simulations and neutron and x-ray scattering experiments. The choice to target the compositions $\text{Ge}_{10}\text{As}_{10}\text{Se}_{80}$ and $\text{Ge}_{21}\text{As}_{21}\text{Se}_{58}$ is related with the purpose of contrasting effects arising from topology from those driven by chemistry. $\text{Ge}_{10}\text{As}_{10}\text{Se}_{80}$ has a network mean coordination number of $\bar{r} = 2.3$ and belongs to the flexible phase [14] where dominant topological effects are expected, i.e., chain cross-linking of Se chains is supposed to drive the overall network properties and a structure that is characterized by a lack of preferential bonding and behaves as a random covalent network

[21]. Conversely, $\text{Ge}_{21}\text{As}_{21}\text{Se}_{58}$ is a composition typical of a stressed-rigid phase having a large connectivity and where chemical disorder (homopolar bondings, nanoscale phase separations [18]) is supposed to dominate.

While a good agreement is obtained between theory and experiment from neutron and x-ray scattering, results from simulations indicate that the structure is dominated by Ge-Se, As-Se, and Se-Se bonds for Se-rich compositions, whereas As-As and As-Ge defect bondings occur at larger network connectivity but leave average quantities (i.e., \bar{r}) globally compatible with expectations from the $8-\mathcal{N}$ rule. The increase of As and Ge content leads to a growth of ring structures that are dominated by edge-sharing motifs (4-membered rings) that contain only heteropolar bonds with the presence of either two Ge atoms or one Ge and one As atom. In order to probe the vibrational isocoordination rule and the claim of a dominant topological character of such ternary networks, results on $\text{Ge}_{10}\text{As}_{10}\text{Se}_{80}$ and $\text{Ge}_{21}\text{As}_{21}\text{Se}_{58}$ are contrasted with previous calculations on $\text{As}_{30}\text{Se}_{70}$ [39] (expected $\bar{r} = 2.30$) and $\text{Ge}_{33}\text{Se}_{67}$ [40,41] ($\bar{r} = 2.67$). Although the isocoordination rule might hold for $\bar{r} = 2.30$ only, the comparison of ring statistics clearly indicates that binary and ternary networks do not exhibit the same topology at all. Finally, an inspection of Bhatia-Thornton structure factors for all systems permits to analyze topological and chemical ordering in these ternaries which shows that the total structure factor is dominated by number-number correlations $S_{NN}(k)$ characterizing topological ordering, albeit these reveal a reduced contribution for the principal peak (usually associated with directional bonding) with respect to the reference binaries.

II. METHODS

A. First-principles molecular dynamics

First-principles molecular dynamics simulations (FPMD) [42] using a canonical (NVT) ensemble were performed on $\text{Ge}_{10}\text{As}_{10}\text{Se}_{80}$ and $\text{Ge}_{21}\text{As}_{21}\text{Se}_{58}$ systems containing $N = 249$ atoms with the number of As, Ge, and Se atoms fulfilling the desired stoichiometry (e.g., $N_{\text{Ge}} = N_{\text{As}} = 25$ for $\text{Ge}_{10}\text{As}_{10}\text{Se}_{80}$). A periodically repeated cubic cell was used, whose size changes according to the number density ρ_0 of the glasses [18] (Fig. 1). We used DFT in combination with plane wave basis sets. The electronic scheme used a BLYP functional [43,44] within a generalized gradient approximation for the exchange correlation energy. Previous investigations on the related binaries Ge-Se [3,45–47] and As-Se [39,48] have shown that this electronic scheme improves substantially the description of both short and intermediate range in the liquid and amorphous state with respect to experiment (scattering). The electronic structure of the As-Ge-Se liquids and glasses was described within DFT and evolved self-consistently during the motion with valence electrons being treated explicitly, in conjunction with norm-conserving pseudopotentials to account for core-valence interactions. The wave functions were expanded at the Γ point of the supercell and the energy cutoff was set at 20 Ry. Starting configurations were taken from binary Ge-Se liquids [40] and As atoms were randomly inserted in order to meet the desired stoichiometry.

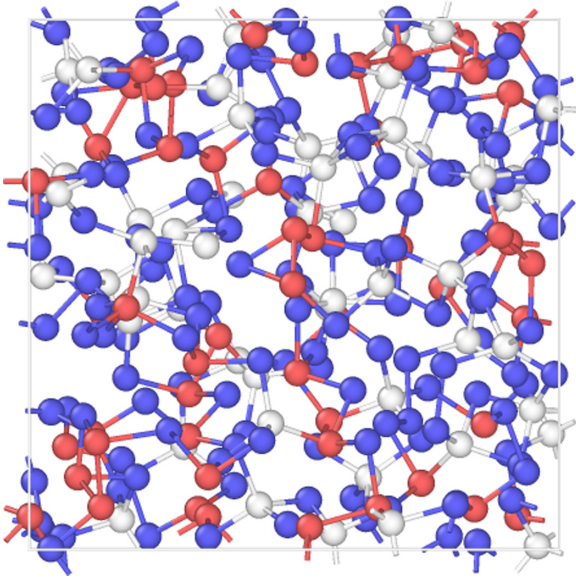


FIG. 1. An example of an obtained amorphous $\text{Ge}_{21}\text{As}_{21}\text{Se}_{58}$ system. Blue, white, and red atoms represent selenium, germanium, and arsenic atoms, respectively.

Loss of the memory of the initial configurations has been achieved through preliminary runs at 2000 K over 50 ps with a time step of $\Delta t = 0.12$ fs and a fictitious mass of 1000 a.u., prior to equilibration at 1500 K, 1200 K, 900 K, and 600 K, each at 20–25 ps, and finally 300 K for 50 ps. Certain properties of the liquid state have been reported elsewhere [18].

B. Sample preparation

$\text{Ge}_{12}\text{As}_{12}\text{Se}_{76}$ and $\text{Ge}_{20}\text{As}_{20}\text{Se}_{60}$ bulk glasses were synthesized using the melt-quenched technique. Note that these are slightly different in composition with respect to FPMD ($\text{Ge}_{10}\text{As}_{10}\text{Se}_{80}$ and $\text{Ge}_{21}\text{As}_{21}\text{Se}_{58}$). A total of 10 g of 5N purity elements were placed in a quartz ampoule, evacuated to 10^{-3} Pa and then sealed. The ampoule was then placed in a rocking furnace heated to 970°C at a rate of $1^\circ\text{C}/\text{min}$, and after reaching the target temperature, the rocking was maintained for 24 h. In the next step, the temperature was reduced to 700°C with a cooling rate of $2^\circ\text{C}/\text{min}$, then the rocking was stopped for 1 h and, finally, the ampoules were quenched in cold water. The bulk glasses in the ampoules were subsequently annealed for 3 hours at about 20°C below the glass transition temperature to release internal stress.

C. Neutron and x-ray scattering experiments

Neutron diffraction (ND) measurements were carried out at the NOVA diffractometer of the 500-kW spallation neutron source of J-PARC, Japan. Powder samples were filled into V-Ni null scattering alloy containers with an outer diameter of 6.0 mm and a thickness of 0.1 mm was used. Each sample was measured for 6 hours. Raw data were corrected for empty instrument background, scattering from the sample holder, multiple scattering, and absorption.

High-energy x-ray diffraction (XRD) data were collected on the Joint Engineering, Environmental and Processing (I12-JEEP) beamline [49] at Diamond Light Source Ltd., the United Kingdom. The sample material was first ground and then loaded into a thin-walled borosilicate capillary of 1.5 mm in diameter. The capillary was illuminated by an x-ray beam of the energy of 100.046 keV and the size of $0.5 \times 0.5 \text{ mm}^2$ for 300 s. The diffracted x-rays were detected by a flat type detector Pilatus 2M CdTe positioned at the distance of 236.6 mm from a sample in transmission geometry. The energy and geometry calibration [50] together with the azimuthal integration of 2D diffraction data into the reciprocal space were performed using the DAWN software [51]. Raw intensity 1D curves were then corrected for the background scattering (an empty capillary and air contributions), sample absorption, fluorescence, and Compton scattering using standard procedures [52] to get only elastically scattered intensities from a sample. Finally, the intensity curves were normalized applying the Faber-Ziman (FZ) formalism [53] to extract structure factors.

III. RESULTS

In Fig. 2 are represented the measured and calculated neutron and x-ray total structure factors $S(k)$. Note again that the theoretical and experimental compositions are close but not identical.

In the simulation, the total weighted structure factors are derived using the partial correlations $S_{nm}(k)$

$$S(k) = \langle f \rangle^{-2} \sum_{n,m} c_n c_m f_n f_m S_{nm}(k) \quad (1)$$

with

$$\langle f \rangle = \sum_n c_n f_n = x_{\text{Ge}} f_{\text{Ge}} + x_{\text{As}} f_{\text{As}} + (1 - x_{\text{Ge}} - x_{\text{As}}) f_{\text{Se}}, \quad (2)$$

where the f_n represent either the atomic form factors ($f_{\text{Ge}} = 32$, $f_{\text{As}} = 33$, and $f_{\text{Se}} = 34$) or the neutron-scattering lengths ($f_{\text{Ge}} = 0.8185$ fm, $f_{\text{As}} = 0.658$ fm, and $f_{\text{Se}} = 0.797$ fm) and c_n represent the species concentration, respectively. The partial correlations and total in Fourier space have been evaluated either directly from the atomic positions (gray curves, Fig. 2),

$$S_{nm}(k) = \frac{1}{N} \left\langle \sum_n \sum_m e^{-i\mathbf{k} \cdot (\mathbf{R}_n - \mathbf{R}_m)} \right\rangle \quad (3)$$

or from a Fourier transform (black curves, Fig. 2) of the partial pair correlation functions $g_{nm}(r)$:

$$S_{nm}(k) = 1 + \rho_0 \int_0^\infty 4\pi r^2 \left[g_{nm}(r) - 1 \right] \frac{\sin(kr)}{kr} dr, \quad (4)$$

where ρ_0 is the system density. The calculated $S(k)$ permits to recover peak positions and appear to be compatible with the measured total structure factor, albeit the intensity of the first-principal peak at $k_2 = 2.09 \text{ \AA}^{-1}$ (and secondary peak at $k_1 = 3.61 \text{ \AA}^{-1}$ to a lesser extent) are slightly underestimated in FPMD simulations. In addition, the minima between the different main peaks at $\approx 1.5 \text{ \AA}^{-1}$ and $\approx 3.0 \text{ \AA}^{-1}$ also appear to be insufficiently reproduced. The behavior up to $k \approx 20 \text{ \AA}^{-1}$

is fairly reproduced and this becomes obvious once the interference function $I(k) = k[S(k) - 1]$ is represented (Fig. 3) as $I(k)$ blows up the oscillations at large scattering vector, the oscillation period being correctly estimated from the calculation. The reasonable agreement at large k is, thus, an indication that the short-range order of the Ge-As-Se networks is correctly reproduced. Furthermore, a recent Gaussian decomposition in Fourier space of $S(k)$ has shown that features beyond the principal peaks (PP) region ($k \geq 7 \text{ \AA}^{-1}$) are linked with second-neighbor correlations [54]. In this respect, the small contribution at $\simeq 7 \text{ \AA}^{-1}$ (barely visible on Fig. 2 but noticeable on Fig. 3) is also reproduced from the simulation and provides some confidence about the obtained structural models. Once considered as a function of Se content, the structure factor evolution exhibits an increased amplitude for the first sharp diffraction peak (FSDP) observed at $k_3 = k_{\text{FSDP}} \simeq 1.0 \text{ \AA}^{-1}$ for, e.g., $\text{Ge}_{20}\text{As}_{20}\text{Se}_{60}$ [Fig. 2(a)]. This feature is typical of cross-linked glasses and compatible with results from a FSDP analysis of binary chalcogenides [55] which concluded that the amplitude of this peak increases with network mean coordination \bar{r} .

Partial correlations have been calculated from the obtained trajectories using Eq. (3) and (4). A typical decomposition is

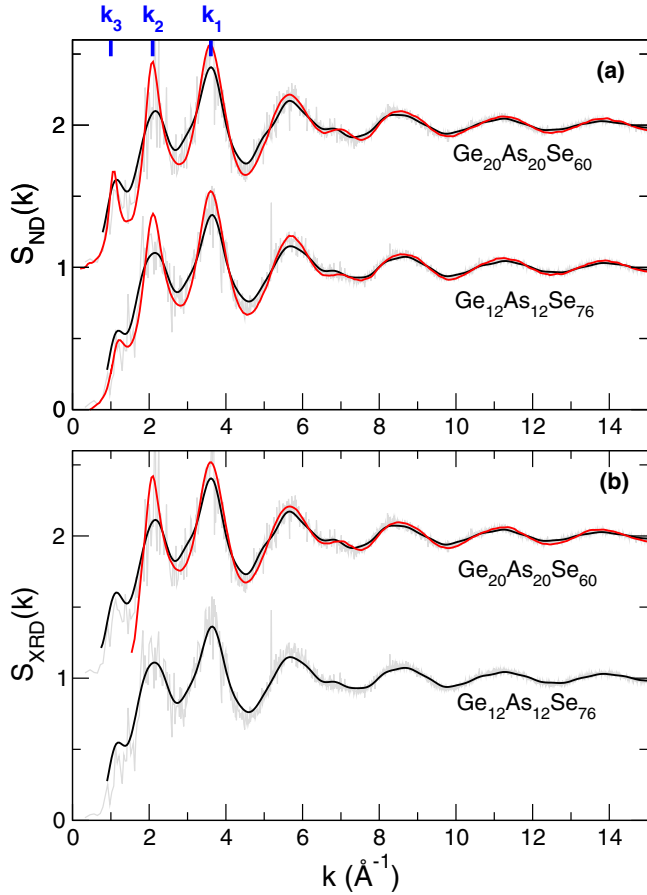


FIG. 2. Measured neutron (a) and x-ray (b) scattering structure factor (red) of $\text{Ge}_{12}\text{As}_{12}\text{Se}_{76}$ and $\text{Ge}_{20}\text{As}_{20}\text{Se}_{60}$ glasses, compared to the corresponding $S_{\text{ND}}(k)$ and $S_{\text{XRD}}(k)$ calculated from FPMD using either Eq. (4) (black) or Eq. (3) (gray). Positions of the principal peaks at k_1 , k_2 , and $k_3 = k_{\text{FSDP}}$ are indicated.

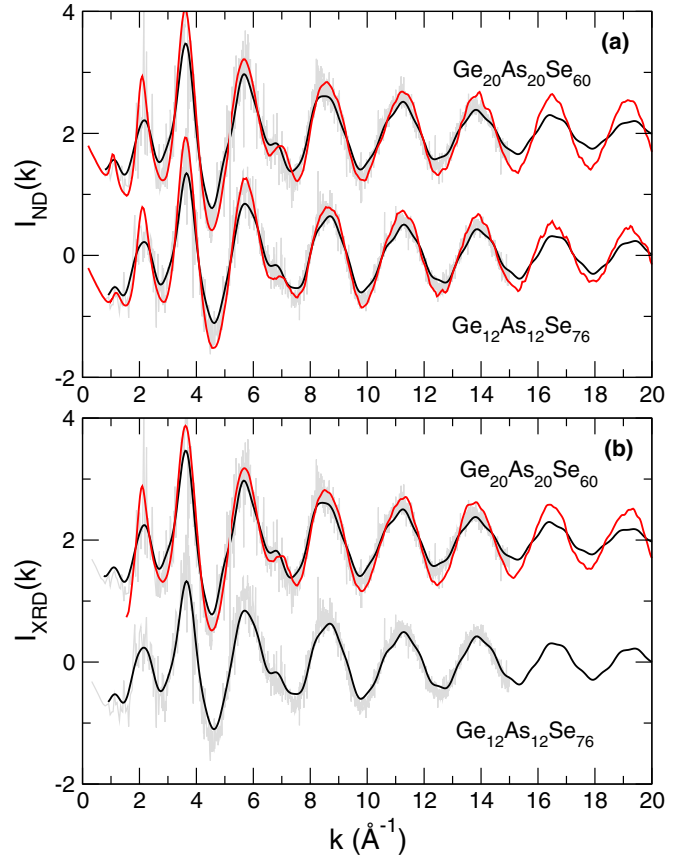


FIG. 3. Measured neutron (a) and x-ray (b) interference function $I(k)$ (red) of $\text{Ge}_{12}\text{As}_{12}\text{Se}_{76}$ and $\text{Ge}_{20}\text{As}_{20}\text{Se}_{60}$ glasses compared to the corresponding calculated $I_{\text{ND}}(k)$ and $I_{\text{XRD}}(k)$ using either Eq. (4) (black) or Eq. (3) (gray).

represented in Fig. 4 and shows that $S(k)$ is essentially made of contributions arising from Ge-Se, As-Se, and Se-Se Faber-Ziman correlations in Fourier space which will dominate even for the largest composition (21%, not shown), as one has, e.g., for XRD weights and $x = 10\%$ [Eq. (5)] and 21% [Eq. (6)], respectively:

$$S(k) = 0.009(0)S_{\text{GeGe}} + 0.018(9)S_{\text{GeAs}} + 0.153(2)S_{\text{GeSe}} \\ + 0.009(6)S_{\text{AsAs}} + 0.158(1)S_{\text{AsSe}} + 0.651(4)S_{\text{SeSe}}, \quad (5)$$

$$S(k) = 0.045(5)S_{\text{GeGe}} + 0.083(6)S_{\text{GeAs}} + 0.282(1)S_{\text{GeSe}} \\ + 0.0431(2)S_{\text{AsAs}} + 0.245(4)S_{\text{AsSe}} + 0.349(2)S_{\text{SeSe}}. \quad (6)$$

Most of the typical features are obviously dominated by the $S_{\text{SeSe}}(k)$ function with PPs at k_2 and k_1 as well as secondary peaks at larger scattering vector k being detected for this partial structure factor (5.8 \AA^{-1} , 8.5 \AA^{-1} , Fig. 4), including the small contribution at $\simeq 7 \text{ \AA}^{-1}$ that is usually the signature of second-shell neighbors of rank $N > n_{\text{Se}}$. However, the FSDP arises essentially from Ge-Se correlations as we find a dominant peak at k_{FSDP} in $S_{\text{GeSe}}(k)$. One should note that all other partials [$S_{\text{GeGe}}(k)$, $S_{\text{GeAs}}(k)$, and $S_{\text{AsAs}}(k)$], once appropriately

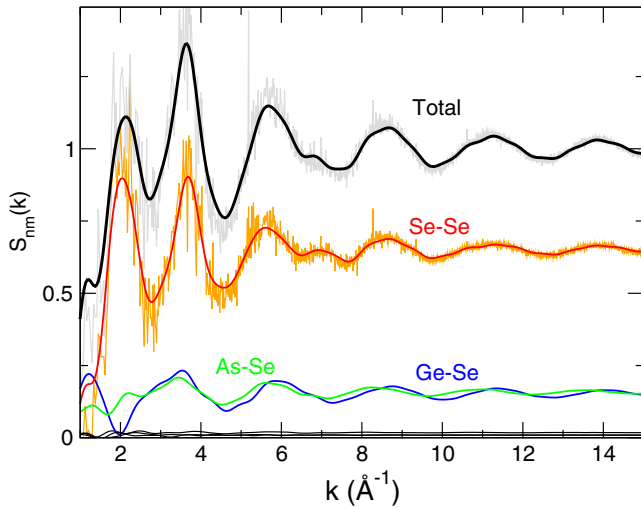


FIG. 4. Decomposition of the total $S(k)$ of $\text{Ge}_{10}\text{As}_{10}\text{Se}_{80}$ [same as Fig. 2(b)] into relevant weighted partials $c_n c_m f_n f_m S_{nm}(k)/\langle f \rangle^2$: Se-Se [red curve using Eq. (4) and orange curve using Eq. (3)], Ge-Se (blue), and As-Se (green). The contribution of the other partials is minimum and barely visible [black curves with $S(k) \leq 0.02$].

weighted, are found to be of about $\simeq 10\text{-}15\%$ of the total only [Eqs. (5) and (6)].

Once the partials $S_{nm}(k)$ of the two systems are being compared (Fig. 5), one detects that the increase of the FSDP amplitude of the total $S(k)$ acknowledged both from experiment and simulations (Fig. 2) must be due to the increase of the corresponding peak in the Ge-Se partial, whereas it is absent in As-Se, this partial $S_{\text{AsSe}}(k)$ being furthermore not influenced by the change in composition, in contrast with the two other partials (Se-Se and Ge-Se) which exhibit obvious changes for $k < 5 \text{ \AA}^{-1}$. The superposition of the oscillations at large scattering vector k between both compounds is the indication that the average short-range order is not altered.

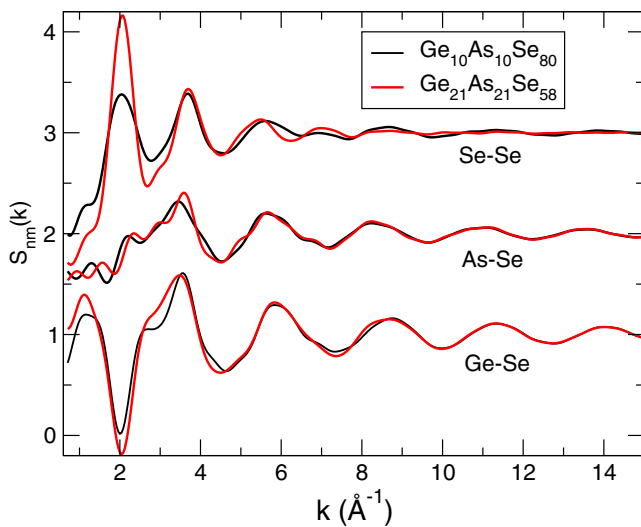


FIG. 5. Decomposition of the total $S(k)$ of $\text{Ge}_{10}\text{As}_{10}\text{Se}_{80}$ (black) and $\text{Ge}_{21}\text{As}_{21}\text{Se}_{58}$ (red) into the main partials: Ge-Se, As-Se, and Se-Se. The curves for As-Se and Se-Se are shifted by +1 and +2 for clarity of presentation.

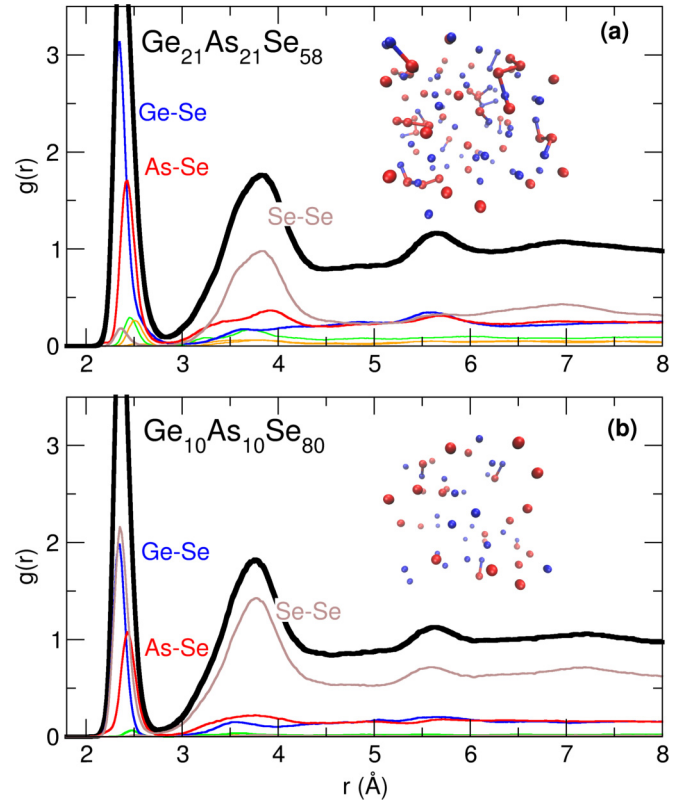


FIG. 6. Decomposition of the total pair correlation function $g(r)$ of $\text{Ge}_{10}\text{As}_{10}\text{Se}_{80}$ (a) and $\text{Ge}_{21}\text{As}_{21}\text{Se}_{58}$ (b) into relevant weighted partials $c_n c_m f_n f_m g_{nm}(r)/\langle f \rangle^2$: Ge-Se (blue), As-Se (red), Se-Se (brown), Ge-As (green), and As-As (orange). Atomic snapshots represent only As (red) and Ge atoms (blue) and permit to highlight the presence of As-As, As-Ge, and Ge-Ge bonds.

A. Real space properties

1. Pair correlations and bond distances

In Fig. 6 are represented the total pair correlation functions $g(r)$ of both systems (thick black curves), together with their weighted partial decomposition. For the chalcogen-rich compound, the principal peak results from a near equivalent contribution of Se-Se, Ge-Se, and As-Se correlations with slightly different bonds lengths (Table I) as it is found 2.35–2.36 Å for Ge-Se and Se-Se bonds (similarly to Ge-Se glasses [47]) but 2.45 Å for As-Se (2.47 Å in $\text{As}_{30}\text{Se}_{70}$ [39]). In this range of distances, the contribution of other partials to the total $g(r)$ appears to be very small (As-As, As-Ge, and Ge-Ge) although the amplitude of corresponding peaks (Table I) grows with decreasing Se content, i.e., Ge-Ge and As-As are

TABLE I. Calculated first correlating distances d_{ij} (Å) compared to data extracted from RMC simulations [21]. The resolution for bond distances is 0.05 Å.

$i-j$	Ge-Ge	Ge-As	Ge-Se	As-As	As-Se	Se-Se
$\text{Ge}_{10}\text{As}_{10}\text{Se}_{80}$		2.49	2.35	2.54	2.45	2.36
RMC [21]	2.39	2.45	2.35	2.39	2.39	2.35
$\text{Ge}_{21}\text{As}_{21}\text{Se}_{58}$	2.55	2.46	2.36	2.51	2.44	2.36

TABLE II. Coordination numbers n_{nm} of the two systems, compared to reference systems $\text{As}_{30}\text{Se}_{70}$ and $\text{Ge}_{30}\text{Se}_{70}$. The values in brackets correspond to random covalent networks.

	$\text{Ge}_{10}\text{As}_{10}\text{Se}_{80}$	$\text{Ge}_{21}\text{As}_{21}\text{Se}_{58}$	$\text{As}_{30}\text{Se}_{70}$ [39]	$\text{Ge}_{33}\text{Se}_{67}$ [47]
n_{GeGe}	(0.70)	0.08		0.25
n_{GeAs}	0.16 (0.52)	0.35		
n_{GeSe}	3.84 (2.78)	3.37		3.55
n_{AsAs}	0.08 (0.39)	0.65	0.07	
n_{AsSe}	2.68 (2.09)	1.97	2.94	
n_{SeSe}	1.17 (1.39)	0.12	0.74	0.30
n_{Ge}	4.00 (4.00)	3.78		3.80
n_{As}	2.92 (3.00)	2.97	3.01	
n_{Se}	1.98 (2.00)	2.03	2.00	2.08
\bar{r}	2.28 (2.30)	2.59 (2.60)	2.30	2.64

virtually absent for $\text{Ge}_{10}\text{As}_{10}\text{Se}_{80}$ [Fig. 6(b)] but clearly visible for $\text{Ge}_{21}\text{As}_{21}\text{Se}_{58}$ [see also snapshots, Fig. 6(a)]. The second-shell essentially arises from Se-Se correlations ($r \simeq 3.8 \text{ \AA}$) which are found on the edges of the $\text{GeSe}_{4/2}$ tetrahedra and the $\text{AsSe}_{3/2}$ pyramid. Indeed, it is easy to check that the typical Se-Se distance involved with Ge atoms satisfies $d_{\text{Se-Se}} = \sqrt{8/3}d_{\text{Ge-Se}}$, i.e., for $\text{Ge}_{21}\text{As}_{21}\text{Se}_{58}$ we find $d_{\text{Ge-Se}} = 2.36 \text{ \AA}$ (Table I) which leads to $d_{\text{Se-Se}} = 3.85 \text{ \AA}$, i.e., identical to the one directly obtained from an inspection of the calculated $g_{\text{Se-Se}}(r)$ (3.84 \AA). The value remains independent of composition which is an indication that no tetrahedral distortion sets in with increasing cross-linking density [56]. We finally note that the calculated bond distances agree with earlier calculations from RMC [21] for the $\text{Ge}_{10}\text{As}_{10}\text{Se}_{80}$ composition, except for the As-As pair which is, however, only present in small amounts (see below).

2. Coordination numbers

In Table II, we have calculated from the partial pair correlation functions $g_{nm}(r)$ the corresponding partial coordination numbers n_{nm} using

$$n_{nm} = 4\pi\rho_0 \int_0^{r_m} r^2 g_{nm}(r) dr, \quad (7)$$

where r_m has been taken at the first minimum of the corresponding partial pair correlation function ($r_m \simeq 2.74 \text{ \AA}$) for nearly all partials. It is noticeable that Se-related coordination numbers decrease from $\text{Ge}_{10}\text{As}_{10}\text{Se}_{80}$ to $\text{Ge}_{21}\text{As}_{21}\text{Se}_{58}$, given the reduction of Se content and the growing presence of As-As and Ge-As bonds that also contribute to the decrease of n_{GeSe} and n_{AsSe} . The total coordination numbers remain nearly constant, however. These have been calculated from:

$$n_m = n_{mm} + \sum_{p \neq m} n_{pm} \quad (8)$$

and, e.g., $x_{\text{Se}}n_{\text{SeGe}} = x_{\text{Ge}}n_{\text{GeSe}}$. Results show that the atoms follow, indeed, the 8- \mathcal{N} rule because Ge atoms have a coordination number of about 3.78–4.00, whereas As and Se atoms have a coordination number that remains close to $n_{\text{As}} = 3$ and $n_{\text{Se}} = 2$, respectively. The detail of bonding types on the calculated statistics of species reveals the presence of defect coordinated Ge atoms in $\text{Ge}_{21}\text{As}_{21}\text{Se}_{58}$ (17.4% Ge^{II}

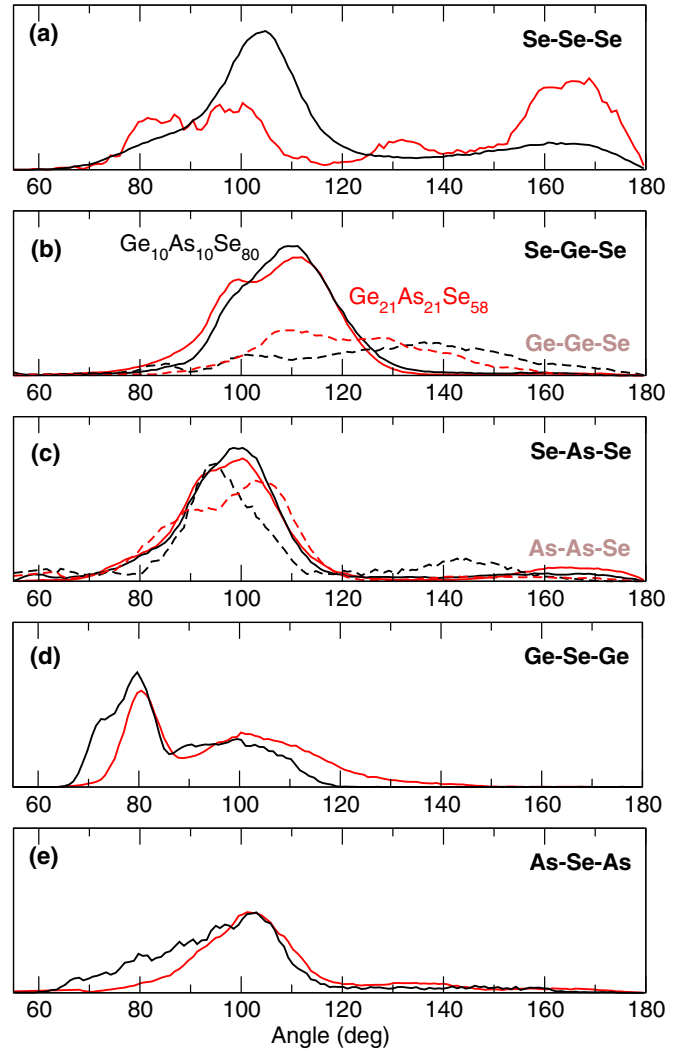


FIG. 7. Calculated bond angle distributions of $\text{Ge}_{10}\text{As}_{10}\text{Se}_{80}$ (black) and $\text{Ge}_{21}\text{As}_{21}\text{Se}_{58}$ (red). Panels (b) and (c) also represent the Ge-Ge-Se and As-As-Se bond angle distributions, respectively (broken curves with same color code as the solid curves).

and 5.8% Ge^{II} , Table III) and twofold As atoms (16% in $\text{Ge}_{10}\text{As}_{10}\text{Se}_{80}$ and 39.4% in $\text{Ge}_{21}\text{As}_{21}\text{Se}_{58}$), both displaying the presence of bonds with As or Ge atoms. Ge-Ge bonds appear to be unlikely ($n_{\text{GeGe}} = 0.08$, Table II) so that $\text{AsGeSe}_{3/2}$ species (013, i.e., 16.0% in $\text{Ge}_{10}\text{As}_{10}\text{Se}_{80}$, 23.1% in $\text{Ge}_{21}\text{As}_{21}\text{Se}_{58}$) or As_2GeSe (022) are being preferred. These features indicate a chemical ordering (i.e., preferential bonding) that appears to be different with related binary glasses.

3. Bond angles

Figure 7 shows the calculated bond angle distributions (BAD) for both systems. Chain segments Se-Se-Se are centered at about 100° [Fig. 7(a)] as in elemental selenium [57], the BAD of $\text{Ge}_{21}\text{As}_{21}\text{Se}_{58}$ being not meaningful due to the near absence of Se-Se-Se segments for this compound. Once Se becomes a linkage between (As,Ge) atoms, the BAD remains nearly centered at the same bond angle (100° – 110°) but with an evolution that eventually reveals the signature of edge-

TABLE III. Calculated fraction (%) of Ge and As having n Ge, m As, and p Se neighbors.

nmp		004	013	022	003	012	002	200	101	102
Ge	Ge ₁₀ As ₁₀ Se ₈₀	84.0	16.0							
	Ge ₂₁ As ₂₁ Se ₅₈	50.0	23.1	3.9	13.5	3.9	5.8			
As	Ge ₁₀ As ₁₀ Se ₈₀				72.0		16.0			8.0
	Ge ₂₁ As ₂₁ Se ₅₈				29.8		29.8	3.9	9.6	11.5

sharing (ES) structures [at 80° in Ge-Se-Ge, Fig. 7(d)] with a bimodal distribution that is also found in binary Ge-Se glasses [47]. It has to be remarked that Ge- and As-centered BADs (Se-As-Se and Se-Ge-Se) remain nearly unchanged with composition [Figs. 7(b) and 7(d)], although one acknowledges for the former a shoulder peak structure for Ge₂₁As₂₁Se₅₈ (red curves) which is also indicative of an increased presence of ES structures that can be verified (i) from the Ge-Se-Ge BAD [Fig. 7(d)] and (ii) from a ring analysis which shows a growing presence of fourfold rings (see below). The Se-Ge-Se and Se-As-Se distributions are peaked at 109° and 98° , respectively, and reveal the tetrahedral geometry for Se-Ge-Se angles centered at $\theta_T = \arccos(-1/3) = 109^\circ$ and the pyramidal geometry for Se-As-Se angles, as also obtained from related binary systems [39,47]. Concerning the latter, one acknowledges for Ge₂₁As₂₁Se₅₈ a small contribution close to 180° which is an indication that the As-centered geometries might be also found in defect octahedral sites as in other pnictide (Group V) chalcogenides [58].

It is also instructive to investigate BADs having a homopolar Ge-Ge or As-Se bond [broken curves in Figs. 7(b) and 7(c)]. The fraction of Ge-Ge bonds being very low (Table I), any definite conclusion of the behavior of Ge-Ge-Se can hardly be drawn, including for the Se-poor composition. Conversely, As-As-Se BADs do display some interesting evolution. The presence of As-As bonds leads, indeed, to a change in the local geometry and, obviously, their presence converts the dominant pyramidal AsSe_{3/2} unit centered at 98° into a possible quasitetrahedral one at large (As,Ge) content as (i) the main peak is found to be shifted to the tetrahedral value θ_T and (ii) the contribution close to 180° vanishes [Fig. 7(c)]. Such features have been detected in simulated As₂Se₃ for which the presence of tetrahedral As was related to the presence of As-As bonds [59].

IV. DISCUSSION

In early studies on the isocoordination rule [2,3,7,8], focus was essentially made on the vibrational density of states and its behavior with the average coordination number \bar{r} for different chalcogenide systems.

A. Vibrational density of states

In order to probe this rule from our obtained models, we have calculated the VDOS $g(\omega)$ using the Fourier transform of the velocity-velocity autocorrelation function:

$$g(\omega) = \frac{1}{Nk_B T} \sum_{j=1}^N \int_{-\infty}^{\infty} \langle \mathbf{v}_j(t) \cdot \mathbf{v}_j(0) \rangle dt. \quad (9)$$

In Fig. 8, we represent the VDOS for Ge₂₁As₂₁Se₅₈ [Fig. 8(a)] and Ge₁₀As₁₀Se₈₀ [Fig. 8(b)] using Eq. (9). For the Se-poor composition ($\bar{r} = 2.60$), we can eventually compare to the reported experimental spectrum of a close composition (Ge₂₃As₁₄Se₆₃ [7]). It is seen that the main features of the VDOS are reproduced and consist in (i) a broad band between 0 and 20 meV usually associated with bond-bending motions [7,60] and corresponding to the transverse acoustic (TA) region, (ii) a second band at 20–25 meV that is slightly underestimated with respect to experiments (peak at 25 meV), and (iii) a high-frequency band associated with stretching vibrations between 20 and 40 meV reminiscent of transverse optic (TO) modes in the crystal. The comparison between both compositions [Figs. 8(a) and 8(b)] indicates a

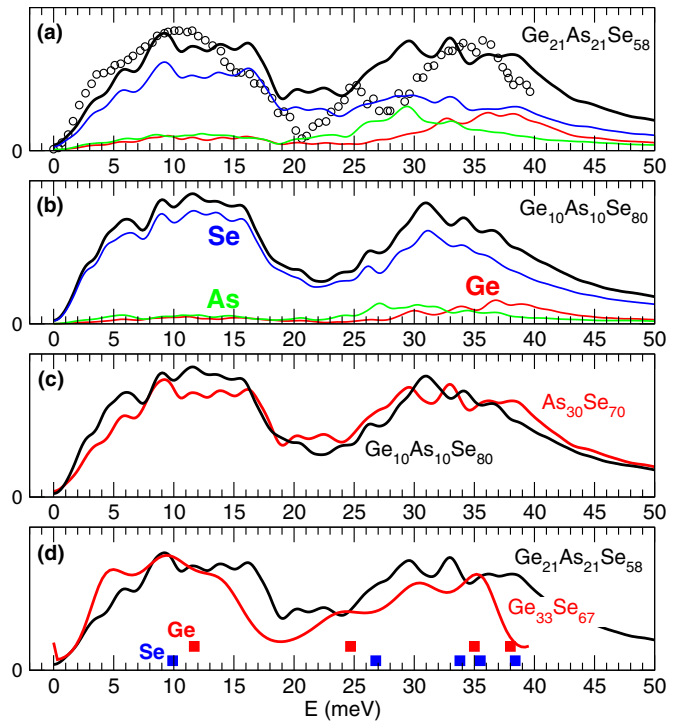


FIG. 8. Calculated VDOS: (a) Ge₂₁As₂₁Se₅₈ and (b) Ge₁₀As₁₀Se₈₀. The total VDOS (black curves) is represented together with weighted contributions from Ge (red), As (green), and Se (blue). Experimental data [7] (circles) correspond to a system with $\bar{r} = 2.60$ (Ge₂₃As₁₄Se₆₃) (c) Comparison of the total calculated VDOS for systems having the same $\bar{r} = 2.3$: Ge₁₀As₁₀Se₈₀ [black, same as (b)] and As₃₀Se₇₀ (red [39]). (d) Comparison of the total calculated VDOS for systems having nearly the same \bar{r} : Ge₂₁As₂₁Se₅₈ (black, $\bar{r} = 2.63$, same as in (a)) and Ge₃₃Se₆₇ (red [47], $\bar{r} = 2.67$). The squares indicate typical modes detected from the experimental Ge- and Se-related partial VDOS of Ge₃₃Se₆₇ [61].

sharpening of the latter with Se content and a more elusive presence of the second band at 20–25 meV for $\text{Ge}_{10}\text{As}_{10}\text{Se}_{80}$. Contributions at high frequency emerge for $\text{Ge}_{21}\text{As}_{21}\text{Se}_{58}$ ($E > 30$ meV) which is the signature of a global stiffening of the network structure. The $\text{Ge}_{10}\text{As}_{10}\text{Se}_{80}$, furthermore, displays an increased amplitude in the region around 5 meV, this particular frequency being assigned to a floppy mode peak clearly visible in a-Se [7]. This is an indication that increased low-frequency modes are present in $\text{Ge}_{10}\text{As}_{10}\text{Se}_{80}$, consistently with the fact that this compound belongs to the flexible phase [7,14,16,18].

1. Contribution from species

Once the contributions of Ge, As, and Se are analyzed, one realizes that both Ge and As lead to vibrations at high frequency (green and red curves), whereas they are absent in the floppy mode region which is essentially dominated by vibrations from Se atoms. These results connect to coherent inelastic neutron scattering with isotope substitution which permits to measure site-specific information on the vibrational dynamics. For $\text{Ge}_{33}\text{Se}_{67}$, it has been found [61] that Ge atoms lead to peaks at 11.7, 24.7, and 38.0 meV and to a shoulder peak at 35 meV [symbols, Fig. 8(d)], whereas Se-related peaks are measured at 9.9 and 26.8 meV together with a broad feature at 33.8, 35.5, and 38.4 meV.

Additional insight is provided from the analysis of local vibrations and typical frequencies of isolated local geometries. Here the electronic DFT scheme is used to determine from an exact diagonalization of the Hessian matrix the vibrational eigenmodes and eigenvectors of $\text{GeSe}_{4/2}$ tetrahedra [47] and $\text{AsSe}_{3/2}$ pyramids [39,62]. The frequency analysis and a visual inspection of the atomic motion offer an assignment to typical bands of the VDOS. Intratetrahedral $\text{GeSe}_{4/2}$ bending modes lead [47] to some typical frequencies in the TA part of the VDOS (8 and 11 meV [63]), whereas stretching modes (the so-called tetrahedral A_1 mode [63,64]) contribute to experimental assignments determined at 12.4, 24.8, and 25.9 meV. The modes found in the upper tail of the TO band (32.2 and 33.7 meV) consist in the reported stretch-antistretch F_2 mode [63]. The pyramid $\text{AsSe}_{3/2}$ has been analyzed in the same fashion [62] and corresponding eigenmodes contribute to bands found in the 8- to 15-meV region and are associated with bending/stretching and/or deformation modes of the local geometry [65], the modes at the largest frequencies (31 meV) giving rise to umbrella flip modes. It should be also mentioned that larger frequencies are obtained in the range $22.3 \text{ meV} \leq E \leq 32.2 \text{ meV}$ when isolated quasitetrahedral $\text{Se} = \text{AsSe}_{3/2}$ are considered [62,66,67]. As $n_{\text{As}} \simeq 3$ (Table I), these geometries do not seem to exist in the present ternaries (see, however, Ref. [18]), and recent simulations have shown that they might be rather unstable, at least in DFT-based simulations [62].

2. Vibrational isocordination rule

In order to check for the validity of the vibrational isocordination rule [2,3], we compare two different chemical systems of nearly the same average coordination number \bar{r} . Figure 8(c) shows the vibrational density of states for $\text{Ge}_{10}\text{As}_{10}\text{Se}_{80}$ (black) compared to $\text{As}_{30}\text{Se}_{70}$ (red [39]), both

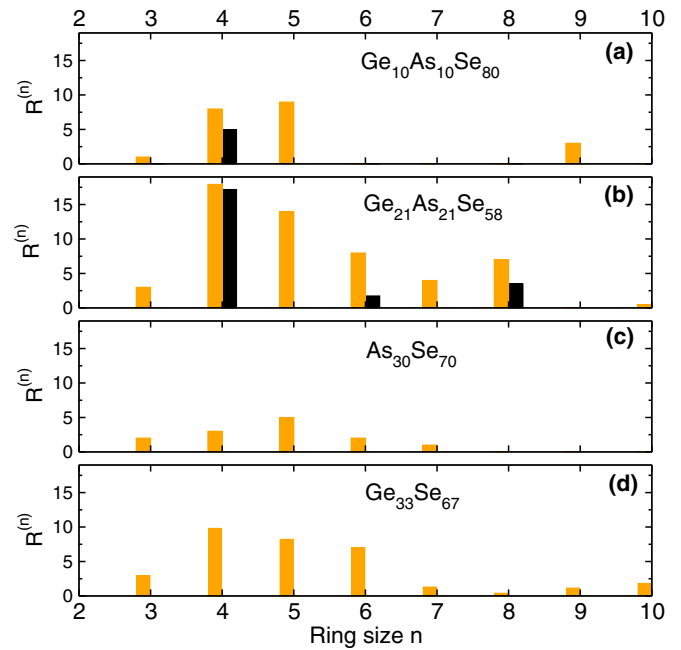


FIG. 9. Calculated ring population (number of rings found divided by the system size N) in $\text{Ge}_{10}\text{As}_{10}\text{Se}_{80}$ (a), $\text{Ge}_{21}\text{As}_{21}\text{Se}_{58}$ (b), $\text{As}_{30}\text{Se}_{70}$ [39] (c), and $\text{Ge}_{33}\text{Se}_{67}$ [47] (d). The calculation focuses either on all rings (orange) or on even rings containing only heteropolar bonds (ABAB rings, black).

having the property $\bar{r} = 2.30$. Similarly, we represent in Fig. 8(d) the VDOS of $\text{Ge}_{21}\text{As}_{21}\text{Se}_{58}$ ($\bar{r} = 2.63$) and $\text{Ge}_{33}\text{Se}_{67}$ [47] ($\bar{r} = 2.67$).

First, we note that the rule is qualitatively valid for $\text{Ge}_{10}\text{As}_{10}\text{Se}_{80}$ as all bands are similar to the one of $\text{As}_{30}\text{Se}_{70}$: TA ($E \leq 20$ meV) and TO bands ($25 \text{ meV} \leq E \leq 40$ meV). The rule is not fulfilled for the Se-poor compositions and there is an obvious blueshift of both TA and TO bands for the reference compound $\text{Ge}_{33}\text{Se}_{67}$ [47]. It is, therefore, tempting to conclude on the nonvalidity of the vibrational isocordination rule for the large cross-linked (i.e., Se-poor) networks.

B. Ring structure

The topological intermediate-range order can be determined using a ring statistics algorithm that builds on a rigorous investigation of networks generated using a simulation code [68]. A cutoff distance of 2.74 Å has been used for all atomic pairs, corresponding to the minimum r_m of the pair distribution functions (Fig. 6). The algorithm is mostly based on the King [69]-Franzblau [70] shortest-path search to find rings containing a maximum of 10 atoms.

1. General features

Figure 9 displays the ring statistics $R(n)$ for the two compositions of interest and for the two related binary glasses [39,47]. As for other chalcogenides where homopolar bonds are present, all sizes n of rings can be found, i.e., both odd- and even-sized rings, in contrast with, e.g., a GeO_2 structure which has only heteropolar bonds and leads solely to even-sized ring distributions [71]. For the Se-rich composition [Fig. 9(a)], the

network is dominated by four- and fivefold rings composed of a majority of Se-Se bonds. Interestingly, when the nature of such motifs is further analyzed, $n = 4$ rings appear to contain essentially heteropolar bonds and correspond to so-called ABAB motifs [72,73] (As-Se or Ge-Se, black bars, Fig. 9). These are clearly not promoted in larger rings such as $n = 6$ or $n = 8$ ones. It should be also noted that the large presence of the fourfold rings is responsible for the typical bimodal BAD Se-Ge-Se and Ge-Se-Ge that has been previously determined (Fig. 7). The increase of (Ge,As) content leads to an overall increased cross-linking tendency (i.e., connectivity \bar{r}) which manifests by a global growth of all types of rings, the distribution remaining dominated by smaller rings having $n \leq 7$, i.e., rings containing either four (ES motifs) or five or six atoms.

2. Network topology contrasted

Does the network structure of the present ternary glasses resembles to the one characterized for binary systems with the same average coordination number \bar{r} ? Figures 9(c) and 9(d) now display the same statistical analysis concerning the ring population for the isocoordinated $\text{As}_{30}\text{Se}_{70}$ and $\text{Ge}_{33}\text{Se}_{67}$. Obviously, correspondences between, e.g., $\text{Ge}_{10}\text{As}_{10}\text{Se}_{80}$ and $\text{As}_{30}\text{Se}_{70}$ remain only at a qualitative level, i.e., an obvious dominant ring size is obtained ($n = 5$ for $\text{Ge}_{10}\text{As}_{10}\text{Se}_{80}$ and $n = 4$ for $\text{Ge}_{21}\text{As}_{21}\text{Se}_{58}$, similarly to the binaries), and some minimum population is acknowledged at $n = 7$. For $\bar{r} = 2.30$ only a limited number of rings are found due to the residual chainlike nature of the network Se backbone which prevents from an important formation of small ($n = 4-7$) and, moreover, intermediate-sized ($n \geq 8$) rings. The comparison indicates, however, that the fraction of ring structures is largely different between both sets, and in ternary glasses the ring population is promoted with respect to $\text{Ge}_{33}\text{Se}_{67}$ as $R^{(4)} \simeq 18$ for $\text{Ge}_{21}\text{As}_{21}\text{Se}_{58}$. This definitely rules out the idea of having networks with different chemical composition but a same network topology [2,7].

3. Link with typical correlating distances

The presence of a rather large fraction of ES rings in $\text{Ge}_{21}\text{As}_{21}\text{Se}_{58}$ (Fig. 9) signals the presence of a typical correlation distance as in binary Ge-Se glasses [13,47]. In this system, three distances emerge usually at 2.43, 3.03, and 3.61 Å and are associated with homopolar Ge-Ge, ES, and corner-sharing tetrahedra [47], respectively [Fig. 10(b)]. Such features are actually also detected in the present ternary and, especially for the Se-poor composition, exemplified in the partial $g_{\text{GeGe}}(r)$. Figure 10(a) shows this pair correlation function (black curve) which clearly has a three-peak structure in the region $2 \text{ \AA} \leq r \leq 4 \text{ \AA}$, the assignment of the corresponding peaks found at 2.57, 3.04, and 3.71 Å being somewhat larger than those obtained in the corresponding binary Ge-Se, at least for the homopolar distance Ge-Ge and the CS distance. Here the larger system density for $\text{Ge}_{21}\text{As}_{21}\text{Se}_{58}$ [18] (0.0343 \AA^{-3} as compared to 0.0334 \AA^{-3} for $\text{Ge}_{33}\text{Se}_{67}$ [13]) cannot account for the increased bonding distances obtained in the ternary. Similarly, the partial $g_{\text{GeAs}}(r)$ also exhibits this three-peak feature and a shoulder peak corresponding to some ES structures is acknowledged [red arrow in Fig. 10(a)]. A visual inspection of atomic snapshots indicates, indeed, that 4-rings can involve

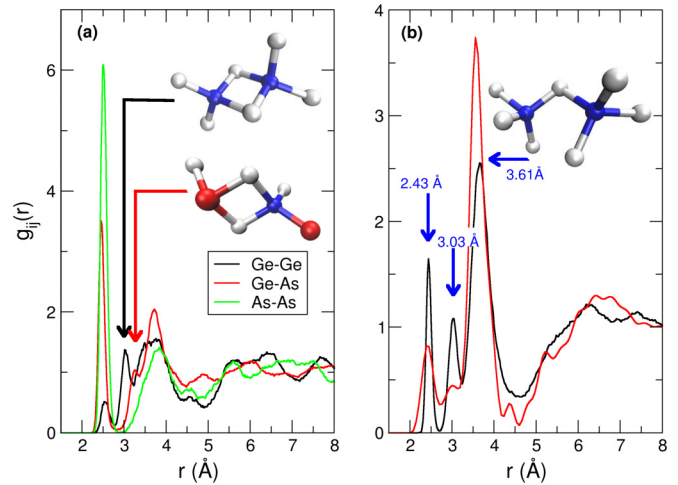


FIG. 10. Pair correlation functions Ge-Ge (black), Ge-As (red), and As-As (green) in $\text{Ge}_{21}\text{As}_{21}\text{Se}_{58}$ (a), and corresponding Ge-Ge pdf (b) in $\text{Ge}_{33}\text{Se}_{67}$ (calculated, black [47], and measured from neutron scattering, red [13]). The molecular structures involve typical correlating Ge-Ge and Ge-As distances marked by arrows (As in red, Ge in blue).

both Ge and As atoms and these lead to a typical correlating distance found at 3.31 Å, and which is clearly distinct from the As-Ge bond at 2.46 Å [first prominent peak in Fig. 10(a) and Table I], both being displayed in a molecular fragment taken from an atomic configuration [Fig. 10(a)]. Conversely, no 4-rings involve two As atoms and this is reflected in the absence of the ES peak in the partial $g_{\text{AsAs}}(r)$ (green curve). This indicates that in ternary glasses, 4-rings are preferentially formed with 100% Ge or 50% Ge and As atoms in a dominant heteropolar configuration (Fig. 9).

C. Topological and chemical ordering

Finally, we examine structure functions which concentrate on long-range topological or chemical ordering of the networks. We use for this purpose the Bhatia-Thornton (BT) formalism which focuses on the number-number correlations (via a corresponding structure factor $S_{NN}^{\text{BT}}(k)$) and concentration-concentration correlations which are given for binary mixtures such as $\text{Ge}_x\text{Se}_{1-x}$ as :

$$S_{\text{CC}}^{\text{BT}}(k) = x_{\text{Ge}}x_{\text{Se}}[1 + S_{\text{GeGe}} + S_{\text{SeSe}} - 2S_{\text{GeSe}}] \quad (10)$$

with S_{ij} the calculated FZ structure factors. The former [$S_{NN}^{\text{BT}}(k)$] probes correlations that are independent of the chemical nature of the scattering centers and, therefore, provides a measure on topological ordering at intermediate and extended length scales [11]. The latter distribution $S_{\text{CC}}^{\text{BT}}(k)$ characterizes how chemical species are distributed over the scattering centers and, thus, gives information on chemical ordering. Note that $S_{\text{CC}}(k)$ converges in the large scattering vector limit to $x_{\text{Ge}}x_{\text{Se}}$. We use here an extension of the formalism to the case of ternary systems [74,75] and can write:

$$S_{NN}^{\text{BT}}(k) = \sum_{i,j} x_i x_j S_{ij}(k) \quad (11)$$

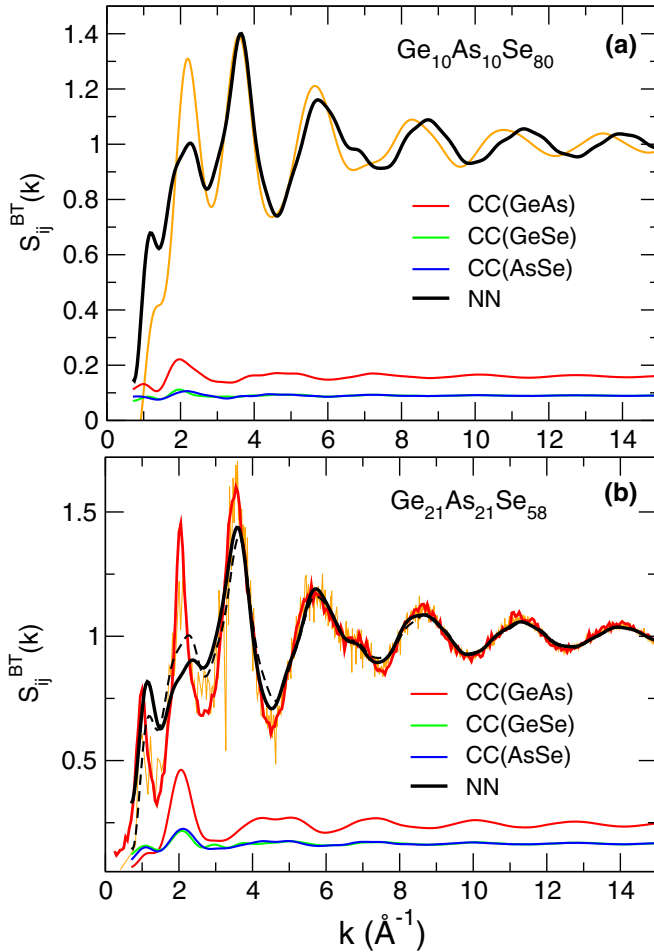


FIG. 11. Calculated BT number-number structure factor $S_{NN}^{\text{BT}}(k)$ and different concentration-concentration structure factors in $\text{Ge}_{10}\text{As}_{10}\text{Se}_{80}$ (a) and $\text{Ge}_{21}\text{As}_{21}\text{Se}_{58}$ (b). Results are being compared to $\text{Ge}_{33}\text{Se}_{67}$ (panel (b), calculated, orange [47]), and measured from neutron scattering, red [13] and $\text{As}_{30}\text{Se}_{70}$ (panel (a), calculated, orange [39]). The broken line in panel (b) is $S_{NN}^{\text{BT}}(k)$ for $\text{Ge}_{10}\text{As}_{10}\text{Se}_{80}$ [same as panel (a)] and serves for comparison.

and for concentration-concentration correlations, we have, e.g.,

$$\begin{aligned}
 x_{\text{Se}}^{-1} S_{\text{CC}(\text{GeAs})}^{\text{BT}}(k) = & x_{\text{Ge}} + x_{\text{As}} + x_{\text{Se}} [x_{\text{Ge}}^2 S_{\text{GeGe}} + x_{\text{As}}^2 S_{\text{AsAs}} \\
 & + 2x_{\text{Ge}}x_{\text{As}}S_{\text{GeAs}} - 2x_{\text{As}}(x_{\text{Ge}} + x_{\text{As}})S_{\text{AsSe}} \\
 & - 2x_{\text{Ge}}(x_{\text{Ge}} + x_{\text{As}})S_{\text{GeSe}} \\
 & + (x_{\text{Ge}} + x_{\text{As}})^2 S_{\text{SeSe}}]. \quad (12)
 \end{aligned}$$

Note that $S_{\text{CC}(\text{GeSe})}^{\text{BT}}(k)$ and $S_{\text{CC}(\text{AsSe})}^{\text{BT}}(k)$ are obtained by a cyclic operation on (Ge,As,Se), and that in the high-wave-vector region k all concentration-concentration structure factors converge to the limit $x_i(x_j + x_k)$ ($i \neq j, k$) which is a direct consequence of the definition of $S_{\text{CC}(\text{GeSe})}^{\text{BT}}(k)$, $S_{\text{CC}(\text{AsSe})}^{\text{BT}}(k)$, and $S_{\text{CC}(\text{GeAs})}^{\text{BT}}(k)$ [Eq. (12)]. Figure 11 now represents both $S_{NN}^{\text{BT}}(k)$ and the different concentration-concentration structure factors for both $\text{Ge}_{10}\text{As}_{10}\text{Se}_{80}$ and $\text{Ge}_{21}\text{As}_{21}\text{Se}_{58}$. These are being compared with the same calculation for the isocoordinated $\text{As}_{30}\text{Se}_{70}$ [39] and $\text{Ge}_{33}\text{Se}_{67}$ [13,47]. The different concentration-concentration functions display a main peak at

the position k_2 , a feature that has been also found for $S_{\text{CC}}^{\text{BT}}(k)$ in different tetrahedral glasses [76], the small peak at $k_3 \simeq 1.0\text{--}1.2 \text{ \AA}^{-1}$ being an indication of concentration fluctuations on intermediate length scales. Results confirm that the “three-peak” character of the structure factor originates from the function focusing on topology [i.e., $S_{NN}^{\text{BT}}(k)$], although notable differences between the intensities are acknowledged with respect to binary As-Se and Ge-Se. One, indeed, immediately observes that the second principal peak at $k_2 \simeq 2.09 \text{ \AA}^{-1}$ is substantially reduced as compared to the related binary glasses, this feature being even more pronounced for the Se-poor composition ($\text{Ge}_{21}\text{As}_{21}\text{Se}_{58}$). It is important to remark that the FPMD underestimation of the peak at k_2 (Fig. 2) cannot entirely account for the present observation.

The peaks found in Bhatia-Thornton provide some information on topological or chemical length scales [77]. The first peak at k_1 has been associated with nearest-neighbor contacts at distance d between species and is therefore a generic feature of all glasses including colloidal materials [78] or series of isochemical glasses ranging from ionic to semimetallic [79]. It is, thus, not surprising that the features of this peak are very similar when the ternary Ge-As-Se compositions (black curves, Fig. 11) are being compared to their binary counterparts [orange curves [39,47] and red curve [13] in Fig. 11(b)]. The amplitude of the correlations in Fourier space [i.e., in $S(k)$] will, indeed, maximize [76,80] at a position given by the Ehrenfest relation $k_1 d = 7.725 \simeq 5\pi/2$ (if one takes here $d = 2.40 \text{ \AA}$, one has $k_1 = 3.21 \text{ \AA}^{-1}$).

The second peak at k_2 emerges only if the bonding scheme assumes a directional character [77] present, e.g., in glassy silica [81] or GeSe_2 [47]. The reason for a reduced intensity at k_2 results from the fact that the ternary glass is made of both tetrahedral and pyramidal motifs. In binary tetrahedral glasses of the form AX_2 (SiO_2 , GeSe_2 , ...), the scattering intensity is found to maximize when the periodicity associated with k_2 is commensurate with a typical distance found, and which is represented by the base-to-apex distance given by $\sqrt{2/3}d_{XX}$ involving the edge (i.e., the $X\text{--}X$ bond distance) of the $\text{AX}_{4/2}$ tetrahedron. Using $d_{XX} = \sqrt{8/3}d_{AX}$, one has therefore $2\pi/k_2 \simeq 4d_{AX}/3$ or $k_2 d_{AX} \simeq 3\pi/2$ at scattering maximum. Here, with $d_{\text{GeSe}} = 2.40 \text{ \AA}$, one has $k_2 = 2.0 \text{ \AA}^{-1}$, i.e., close to the exact location of second principal peak (2.09 \AA^{-1}) but the reduced intensity at this scattering vector indicates an obvious reduced ordering for this particular distance.

V. SUMMARY AND CONCLUSIONS

Glass network-forming chalcogenides not only represent materials of special importance given their possibilities in optoelectronic applications but they are also driven by fundamental features that influence structural characteristics.

Here, using neutron and x-ray scattering experiments together with first-principles molecular dynamics simulations, we have focused on the structural and vibrational properties of two systems able to serve as a probe for the isocoordination rule [2,3]. This rule states that various glass properties only depend solely on an averaged quantity of topological character, that is, the network mean coordination number \bar{r} . Results have been contrasted with isocoordinated binary systems such as $\text{As}_{30}\text{Se}_{70}$ and $\text{Ge}_{33}\text{Se}_{67}$. The study first indicates that the

experimental structure factor can be reproduced from molecular simulations with a rather satisfying accuracy. This permits the validation of the structure models prior to further analysis of structural features.

The molecular simulations reveal that the networks are dominated by fourfold Ge, twofold Se, and threefold As as in corresponding binary glasses. For Se-poor compositions, preferential bonding does occur because As-As homopolar bonds dominate together with As-Ge bonds, the fraction of Ge-Ge being very low. The rest of the network is dominated by Ge-Se, As-Se, and Se-Se bonds whose population depends on composition. Topological ordering manifests by an increased population of heteropolar ES with either two Ge atoms or one Ge and one As atom. A comparison of the ring statistics with corresponding binary glasses (Ge-Se and As-Se) permits to rule out the possibility of a similar topology for the same \bar{r} . This conclusion is also met for the vibrational properties as the VDOS and the so-called isocoordinated rule is merely satisfied for the Se-rich composition.

Taken together, these results highlight the complexity of such ternary networks which bear a similar short-range order with corresponding Ge-Se and As-Se glasses but display profound differences in bonding and intermediate

range order, the latter being captured by ring statistics and Bhatia-Thornton structure functions. As these model structures reproduce with a certain accuracy experimental structure functions accessed from scattering, it would certainly be interesting to focus on other compositions and particularly on those for which anomalies in relaxation behavior are observed [18], in order to establish a neat structure-property relationship as in previous studies on binary glasses [39,47].

ACKNOWLEDGMENTS

This work was carried out with the support of Diamond Light Source, instrument I12-JEEP (nt28087-1). M.K., V.P., and T.W. thank the Czech Science Foundation (Grant No. 20-23392J) and the Ministry of Education, Youth and Sports (LM2018103). M.M. acknowledges access to the supercomputer Roméo of Université de Reims Champagne-Ardenne. Financial support from the Eötvös Loránd Research Network (“ELKH”, Hungary), via their special fund, Grant No. SA-89/2021, is also acknowledged. Neutron scattering experiment was approved by Neutron Scattering Program Advisory Committee of J-PARC MLF (Proposal No. 2019A0161).

-
- [1] *Amorphous Chalcogenides: Structure, Properties, Modeling and Applications*, edited by A. V. Kolobov and K. Shimakawa (World Scientific, Singapore, 2020).
- [2] R. L. Cappelletti, M. Cobb, D. A. Drabold, and W. A. Kamitakahara, *Phys. Rev. B* **52**, 9133 (1995).
- [3] B. Effey and R. L. Cappelletti, *Phys. Rev. B* **59**, 4119 (1999).
- [4] A. N. Sreeram, D. R. Swiler, and A. K. Varshneya, *J. Non-Cryst. Solids* **127**, 287 (1991).
- [5] R. Böhmer and C. A. Angell, *Phys. Rev. B* **45**, 10091 (1992).
- [6] M. Tatsumisago, B. L. Halfpap, J. L. Green, S. M. Lindsay, and C. A. Angell, *Phys. Rev. Lett.* **64**, 1549 (1990).
- [7] W. A. Kamitakahara, R. L. Cappelletti, P. Boolchand, B. Halfpap, F. Gompf, D. A. Neumann, and H. Mutka, *Phys. Rev. B* **44**, 94 (1991).
- [8] N. Mousseau and D. A. Drabold, *Eur. Phys. J. B* **17**, 667 (2000).
- [9] T. Wang, W. H. Wei, X. Shen, R. P. Wang, B. Luther-Davies, and I. Jackson, *J. Phys. D: Appl. Phys.* **46**, 165302 (2013).
- [10] A. Zeidler, P. S. Salmon, D. A. J. Whittaker, K. J. Pizzey, and A. C. Hannon, *Front. Mater.* **4**, 32 (2017).
- [11] P. S. Salmon, R. A. Martin, P. E. Mason, and G. J. Cuello, *Nature (Lond.)* **435**, 75 (2005).
- [12] P. S. Salmon, *J. Phys.: Condens. Matter* **19**, 455208 (2007).
- [13] P. S. Salmon, *J. Non-Cryst. Solids* **353**, 2959 (2007).
- [14] M. Micoulaut, *Adv. Phys. X* **1**, 147 (2016).
- [15] J. C. Phillips, *J. Non-Cryst. Solids* **34**, 153 (1979).
- [16] M. F. Thorpe, *J. Non-Cryst. Solids* **57**, 355 (1983).
- [17] J. C. Maxwell, *Lond. Edinb. Dubl. Philos. Mag. J. Sci.* **27**, 294 (1864).
- [18] R. Chbeir, M. Bauchy, M. Micoulaut, and P. Boolchand, *Front. Mater.* **6**, 173 (2019).
- [19] Z. Černošek, E. Černosková, R. Todorov, and J. Holubová, *J. Solid State Chem.* **291**, 121599 (2020).
- [20] I. Kaban, P. Jóvári, R. P. Wang, B. Luther-Davies, N. Mattern, and J. Eckert, *J. Phys.: Condens. Matter* **24**, 385802 (2012).
- [21] I. Pethes, I. Kaban, R. P. Wang, B. Luther-Davies, and P. Jóvári, *J. Alloys Compd.* **623**, 454 (2015).
- [22] S. W. Xu, R. P. Wang, Z. Y. Yang, L. Wang, and B. Luther-Davies, *Chin. Phys. B* **25**, 057105 (2016).
- [23] D. Chalyy, M. Shpotyuk, R. Golovchak, S. Ubizskii, and O. Shpotyuk, *J. Phys. Stud.* **16**, 1601 (2012).
- [24] C. J. Zha, R. P. Wang, A. Smith, A. Prasad, R. A. Jarvis, and B. Luther-Davies, *J. Mater. Sci.: Mater. Electr.* **18**, 389 (2007).
- [25] R. P. Wang, A. Smith, A. Prasad, D. Y. Choi, and B. Luther-Davies, *J. Appl. Phys.* **106**, 043520 (2009).
- [26] Y. Yang, B. Zhang, A. P. Yang, Z. Y. Yang, and P. Lucas, *J. Phys. Chem. B* **119**, 5096 (2015).
- [27] Y. Wang, P. Boolchand, and M. Micoulaut, *Europhys. Lett.* **52**, 633 (2000).
- [28] E. Mammadov, P. C. Taylor, A. Reyes, S. Mehdiyeva, and P. Kuhns, *Phys. Status Solidi (a)* **207**, 635 (2010).
- [29] R. P. Wang, C. J. Zha, A. V. Rode, S. J. Madden, and B. Luther-Davies, *J. Mater. Sci.: Mater. Electr.* **18**, 419 (2007).
- [30] T. Wang, O. Gulbiten, R. P. Wang, Z. Y. Yang, A. Smith, B. Luther-Davies, and P. Lucas, *J. Phys. Chem. B* **118**, 1436 (2014).
- [31] T. Qu, D. G. Georgiev, P. Boolchand, and M. Micoulaut, *Supercooled Liquids, Glass Transition and Bulk Metallic Glasses*, edited by T. Egami, A. L. Greer, A. Inoue, S. Ranganathan, Vol. 754 (Materials Research Society, Warrendale, PA, 2003).
- [32] O. N. Bolebrukh, N. Y. Sinyavsky, I. P. Korneva, B. Dobosz, M. Ostafin, B. Nogaj, and R. Krzyminiowski, *Central Eur. J. Phys.* **11**, 1686 (2013).
- [33] F. Xia, S. Baccaro, W. Wang, L. Pilloni, X. G. Zhang, H. D. Zeng, and G. R. Chen, *J. Non-Cryst. Solids* **354**, 1137 (2008).
- [34] P. Boolchand, D. G. Georgiev, T. Qu, F. Wang, and L. Cai, *Compt. Rend. Chim.* **5**, 713 (2002).
- [35] M. Micoulaut, *Phys. Rev. B* **74**, 184208 (2006).

- [36] J. Barré, A. R. Bishop, T. Lookman, and A. Saxena, *Phys. Rev. Lett.* **94**, 208701 (2005).
- [37] B. Mantisi, M. Bauchy, and M. Micoulaut, *Phys. Rev. B* **92**, 134201 (2015).
- [38] G. Opletal, R. P. Wang, and S. P. Russo, *Phys. Chem. Chem. Phys.* **15**, 4582 (2013).
- [39] M. Bauchy, A. Kachmar, and M. Micoulaut, *J. Chem. Phys.* **141**, 194506 (2014).
- [40] C. Yildirim, J.-Y. Raty, and M. Micoulaut, *Nat. Commun.* **7**, 11086 (2016).
- [41] C. Yildirim, M. Micoulaut, P. Boolchand, I. Kantor, O. Mathon, J.-P. Gaspard, T. Irifune, and J.-Y. Raty, *Sci. Rep.* **6**, 27317 (2016).
- [42] R. Car and M. Parrinello, *Phys. Rev. Lett.* **55**, 2471 (1985).
- [43] A. D. Becke, *Phys. Rev. A* **38**, 3098 (1988).
- [44] C. Lee, W. Yang, and R. G. Parr, *Phys. Rev. B* **37**, 785 (1988).
- [45] M. Micoulaut, R. Vuilleumier, and C. Massobrio, *Phys. Rev. B* **79**, 214205 (2009).
- [46] C. Massobrio, M. Micoulaut, and P. S. Salmon, *Solid State Sci.* **12**, 199 (2010).
- [47] M. Micoulaut, A. Kachmar, M. Bauchy, S. Le Roux, C. Massobrio, and M. Boero, *Phys. Rev. B* **88**, 054203 (2013).
- [48] M. Bauchy and M. Micoulaut, *J. Non-Cryst. Solids* **377**, 34 (2013).
- [49] M. Drakopoulos, T. Connolley, C. Reinhard, R. Atwood, O. Magdysyuk, and N. Vo, *J. Synchr. Radiat.* **22**, 828 (2015).
- [50] M. L. Hart, M. Drakopoulos, C. Reinhard, and T. Connolley, *J. Appl. Crystallogr.* **46**, 1249 (2013).
- [51] J. Filik, A. W. Ashton, P. C. Y. Chang, P. A. Chater, S. J. Day, and M. Drakopoulos, *J. Appl. Crystallogr.* **50**, 959 (2017).
- [52] T. Egami and S. J. L. Billinge, *Underneath the Bragg Peaks: Structural Analysis of Complex Materials* (Pergamon, Oxford, 2003).
- [53] T. E. Faber and J. M. Ziman, *Philos. Mag.* **11**, 153 (1965).
- [54] M. Micoulaut, *J. Phys.: Condens. Matter* **31**, 285402 (2019).
- [55] E. Bychkov, C. J. Benmore, and D. L. Price, *Phys. Rev. B* **72**, 172107 (2005).
- [56] M. Micoulaut, *J. Phys.: Condens. Matter* **16**, L131 (2004).
- [57] J. Hegedüs, and S. Kugler, *J. Phys.: Condens. Matter* **17**, 6459 (2005).
- [58] M. Micoulaut and H. Flores-Ruiz, *Phys. Rev. B* **103**, 134206 (2021).
- [59] S. Hosokawa, A. Koura, J.-F. Béjar, W.-C. Pilgrim, S. Kohara, and F. Shimojo, *Europhys. Lett.* **102**, 66008 (2013).
- [60] P. Boolchand, R. N. Enzweiler, R. L. Cappelletti, W. A. Kamitakahara, Y. Cai, and M. F. Thorpe, *Solid State Ion.* **39**, 81 (1990).
- [61] D. A. J. Whittaker, L. Giacomazzi, D. Adroja, S. M. Bennington, A. Pasquarello, and P. S. Salmon, *Phys. Rev. B* **98**, 064205 (2018).
- [62] M. Micoulaut and P. Boolchand, *Front. Mater.* **6**, 283 (2019).
- [63] N. Kumagai, J. Shirafuji, and Y. Inuishi, *J. Phys. Soc. Jpn.* **42**, 1262 (1977).
- [64] U. Walter, D. L. Price, S. Susman, and K. J. Volin, *Phys. Rev. B* **37**, 4232 (1988).
- [65] G. Lucovsky, R. J. Nemanich, S. A. Solin, and R. C. Keezer, *Solid State Commun.* **17**, 1567 (1975).
- [66] S. Ravindren, K. Gunasekera, Z. Tucker, A. Diebold, P. Boolchand, and M. Micoulaut, *J. Chem. Phys.* **140**, 134501 (2014).
- [67] K. A. Jackson, A. Briley, S. Grossman, D. V. Porezag, and M. R. Pederson, *Phys. Rev. B* **60**, R14985 (1999).
- [68] S. Le Roux and P. Jund, *Comp. Mater. Sci.* **49**, 70 (2010); **50**, 1217 (2011).
- [69] V. King, *Nature (Lond.)* **213**, 1112 (1967).
- [70] D. S. Franzblau, *Phys. Rev. B* **44**, 4925 (1991).
- [71] M. Micoulaut, X. Yuan, and L. W. Hobbs, *J. Non-Cryst. Solids* **353**, 1961 (2007).
- [72] J. Akola and R. O. Jones, *Phys. Rev. B* **79**, 134118 (2009).
- [73] H. Flores-Ruiz, M. Micoulaut, M.-V. Coulet, A. A. Piarristeguy, M. R. Johnson, G. J. Cuello, and A. Pradel, *Phys. Rev. B* **92**, 134205 (2015).
- [74] J. Blétry, *Z. Naturforsch.* **31**, 960 (1976).
- [75] B. Grosdidier, *J. Non-Cryst. Solids* **525**, 119569 (2019).
- [76] P. S. Salmon, *Proc. R. Soc. A* **445**, 351 (1994).
- [77] P. S. Salmon and A. Zeidler, *J. Stat. Mech.* (2019) 114006.
- [78] P. Wochner, C. Gutt, T. Autenrieth, T. Demmer, V. Bugaev, A. D. Ortiz, A. Duri, F. Zontone, G. Grübel, and H. Dosch, *Proc. Natl. Acad. Sci. USA* **106**, 11511 (2009).
- [79] M. Micoulaut, H. Flores-Ruiz, A. Pradel, and A. Piarristeguy, *Phys. Stat. Solid. B* **15**, 2000490 (2020).
- [80] C. D. Champeney, *Fourier Transforms and Their Physical Applications* (Academic Press, London, 1973).
- [81] S. Kohara, M. Shiga, Y. Onodera, H. Masai, A. Hirata, M. Murakami, T. Morishita, K. Kimura, and K. Hayashi, *Sci. Rep.* **11**, 22180 (2021).